



Article

# Comparison of the Properties of Ni–Mn Hydroxides/Oxides with Ni–Mn Phosphates for the Purpose of Hybrid Supercapacitors

Lyubomir Sosarov <sup>1</sup>, Delyana Marinova <sup>2</sup> , Violeta Koleva <sup>2</sup> , Antonia Stoyanova <sup>1</sup> and Radostina Stoyanova <sup>2,\*</sup>

<sup>1</sup> Institute of Electrochemistry and Energy Systems, Bulgarian Academy of Sciences, Acad. G. Bonchev Str., Bldg. 10, 1113 Sofia, Bulgaria; l\_stefanov@iees.bas.bg (L.S.); antonia.stoyanova@iees.bas.bg (A.S.)

<sup>2</sup> Institute of General and Inorganic Chemistry, Bulgarian Academy of Sciences, Acad. G. Bonchev Str., Bldg. 11, 1113 Sofia, Bulgaria; manasieva@svr.igic.bas.bg (D.M.); vkoleva@svr.igic.bas.bg (V.K.)

\* Correspondence: radstoy@svr.igic.bas.bg; Tel.: +35-9979-3915

**Abstract:** This study aims to quantify the synergistic effect of  $\text{Ni}^{2+}$  and  $\text{Mn}^{2+}$  ions on the capacitive performance of oxide, hydroxide and phosphate electrodes in alkaline electrolytes. Three types of phases containing both nickel and manganese in a ratio of one-to-one were selected due to their stability in alkaline media: oxides with ilmenite and spinel structures ( $\text{NiMnO}_3$  and  $\text{Ni}_{1.5}\text{Mn}_{1.5}\text{O}_4$ ); hydroxides with layered structures ( $\beta\text{-Ni}_{1/2}\text{Mn}_{1/2}(\text{OH})_2$ ); and phosphates with olivine and maricite structures ( $\text{LiNi}_{1/2}\text{Mn}_{1/2}\text{PO}_4$  and  $\text{NaNi}_{1/2}\text{Mn}_{1/2}\text{PO}_4$ ). In the mixed hydroxides and phosphates,  $\text{Ni}^{2+}$  and  $\text{Mn}^{2+}$  ions randomly occupied one crystallographic site, whereas in the ilmenite oxide, a common face was shared by the  $\text{Ni}^{2+}$  and  $\text{Mn}^{4+}$  ions. The electrochemical parameters of the Ni–Mn compositions were evaluated in asymmetric hybrid supercapacitor cells working with alkaline electrolytes and activated carbon as a negative electrode. A comparative analysis of oxides, hydroxides and phosphates enabled us to differentiate the effects of nickel and manganese ions, structures and morphologies on their capacitive performance. Thus, the best performed electrode was predicted. The electrode composition should simultaneously contain Ni and Mn ions, and their morphologies should comprise spherical aggregates. This was an ilmenite  $\text{NiMnO}_3$ , which delivers high energy and power density (i.e.,  $65 \text{ W h kg}^{-1}$  at  $3200 \text{ W kg}^{-1}$ ) and exhibits a good cycling stability (i.e., around 96% after 5000 cycles at a current load of  $240 \text{ mA g}^{-1}$ ).

**Keywords:** hybrid supercapacitors; Ni/Mn oxides; hydroxides and phosphates; synergetic effect; capacitance performance; alkaline electrolyte



**Citation:** Sosarov, L.; Marinova, D.; Koleva, V.; Stoyanova, A.; Stoyanova, R. Comparison of the Properties of Ni–Mn Hydroxides/Oxides with Ni–Mn Phosphates for the Purpose of Hybrid Supercapacitors. *Batteries* **2022**, *8*, 51. <https://doi.org/10.3390/batteries8060051>

Academic Editors: Xia Lu and  
Xueyi Lu

Received: 29 April 2022

Accepted: 24 May 2022

Published: 30 May 2022

**Publisher's Note:** MDPI stays neutral with regard to jurisdictional claims in published maps and institutional affiliations.



**Copyright:** © 2022 by the authors. Licensee MDPI, Basel, Switzerland. This article is an open access article distributed under the terms and conditions of the Creative Commons Attribution (CC BY) license (<https://creativecommons.org/licenses/by/4.0/>).

## 1. Introduction

The elaboration of hybrid supercapacitors with improved energy density and cycling stability is a current challenge that requires identification of the most suitable electrode materials [1–4]. In this context, transitional metal oxides or hydroxides are considered as attractive electrode materials due to their capability to store energy by different mechanisms [1,5–10]. For example,  $\text{MnO}_2$  displays a classical pseudocapacitive mechanism based on fast surface redox reactions with the participation of  $\text{Mn}^{3+}$  and  $\text{Mn}^{4+}$  ions [5,6], whereas  $\text{Ni}(\text{OH})_2$  is characterized by reversible electrochemical redox reactions with  $\text{Ni}^{2+}/\text{Ni}^{3+}$  pair which is concomitant with ion/molecule intercalation [7–10]. The electrochemical storage mechanisms become more diverse when ternary metal oxides/hydroxides having multiple oxidation states are used. According to A/B/O notation, ternary metal compounds can be categorized mainly into three groups:  $\text{AB}_2\text{O}_4$ ,  $\text{ABO}_{2/3/4}$  and  $\text{A}_3\text{B}_2\text{O}_8$  [11,12]. In comparison with  $\text{MnO}_2$ , mixed nickel manganese oxide ( $\text{NiMn}_2\text{O}_4$ ) stored in aqueous electrolytes (e.g., 1 M  $\text{Na}_2\text{SO}_4$ ), the vast majority of capacitance (91%) is by intercalation, and only 9% is by a capacitive mechanism [13]. The performance of oxides depends also on the type of the crystal structure; it has been found that  $\text{NiMnO}_3$  with an ilmenite structure

outperforms  $\text{NiMn}_2\text{O}_4$  with a spinel structure [14]. The ratio between Ni and Mn is also of importance [15,16]; the best capacitive properties have been established for Ni–Mn oxide with Ni:Mn = 1:3. The replacement of oxides with hydroxides has a positive impact on the electrochemical performance of mixed nickel manganese compounds [17,18]. Layered double hydroxides (Ni–Mn LDH), as well as Ni–Mn LDH deposited on reduced graphene oxide, exhibit high faradaic pseudocapacitance, which makes them attractive electrodes for hybrid supercapacitors [12,17,18].

The improved storage performance of mixed Ni–Mn oxides/hydroxides is directly related with the synergistic effect of Ni and Mn ions [19]. The next question is whether the Ni/Mn effect is specific for oxides/hydroxides. In this context, phosphate compounds represent an alternative towards oxides/hydroxides due to their stability in aqueous and carbonate-based electrolytes [20]. Irrespective of this, intensive studies on phosphate-based supercapacitors started in 2012 with  $\text{NH}_4\text{CoPO}_4 \cdot \text{H}_2\text{O}$  [21,22]. Regarding alkaline transition metal phosphates, the first report appeared in 2015, with the electrode being lithium manganese phosphate,  $\text{LiMnPO}_4$ , with an olivine-type structure [23,24]. It has been found that nano-crystalline  $\text{LiMnPO}_4$  coated with a thick carbon layer delivers high capacitance when lithium aqueous electrolytes (such as  $\text{LiOH}$  and  $\text{Li}_2\text{SO}_4$ ) are used. This phospho-olivine shows non-faradic behavior in neutral aqueous electrolytes, whereas in alkaline electrolytes, the faradic kind of the capacitive profiles is more pronounced. Furthermore, the capacitive performance of the phospho-olivine is amplified when the composite between  $\text{LiMnPO}_4$  and reduced graphene oxide aerogel is formed [25]. Like  $\text{LiMnPO}_4$ , nickel analogue  $\text{LiNiPO}_4$  stores electrochemical energy by faradaic and non-faradaic mechanisms [26]. Recently, it has been reported that sodium manganese and sodium nickel phosphates ( $\text{NaMnPO}_4$  and  $\text{NaNiPO}_4$ ) have maricite structures that operate through the same mechanisms in  $\text{NaOH}$  electrolytes; battery-like reversible redox processes are owed to  $\text{Mn}^{2+}/\text{Mn}^{3+}$  and  $\text{Ni}^{2+}/\text{Ni}^{3+}$  redox pairs concomitant with adsorption/desorption reactions at the electrode/electrolyte interface [27–29]. In neutral electrolytes, such as  $\text{NaCl}$  and  $\text{Na}_2\text{SO}_4$ , however, the non-faradaic mechanism prevails [27]. The nickel compound  $\text{NaNiPO}_4$  displays higher specific capacitance than the manganese one,  $\text{NaMnPO}_4$ , with a voltametric specific capacitance of  $390 \text{ F g}^{-1}$  vs.  $219 \text{ F g}^{-1}$  at a scan rate of  $2 \text{ mV s}^{-1}$  [27]. Mixed sodium manganese-nickel-cobalt phosphate (i.e.,  $\text{NaMn}_{1/3}\text{Ni}_{1/3}\text{Co}_{1/3}\text{PO}_4$ ) demonstrates stable capacitive performance in hybrid supercapacitors irrespective of the kind used electrolytes (i.e., 2 M  $\text{NaOH}$  solution and 1 M  $\text{NaPF}_6$  in EC/DEC/DMC) [30,31]. Regardless of these few reports, the capacitive performance of phosphates is still far from that which is desired. That is why the challenge is how to improve the capacitive performance of phosphates.

This study aims to quantify the synergistic effect of nickel and manganese ions on the capacitive performance of oxide, hydroxide and phosphate electrodes in alkaline electrolytes. For all electrodes, the ratio of Ni-to-Mn was selected to be one-to-one. Two types of phosphate phases stable in alkaline media were selected:  $\text{LiNi}_{1/2}\text{Mn}_{1/2}\text{PO}_4$  with an olivine structure and  $\text{NaNi}_{1/2}\text{Mn}_{1/2}\text{PO}_4$  with a maricite structure. As a measure of the phosphate performance, mixed Ni–Mn oxides with ilmenite and spinel structures, as well as mixed Ni–Mn hydroxides with layered structures, were used as references. For the phosphates and hydroxides,  $\text{Ni}^{2+}$  and  $\text{Mn}^{2+}$  ions randomly occupied one crystallographic site, whereas in the ilmenite oxide, a common face was shared by  $\text{Ni}^{2+}$  and  $\text{Mn}^{4+}$  ions (Figure 1).

The electrochemical parameters were evaluated in hybrid supercapacitor cells working with alkaline electrolytes and activated carbon as a negative electrode [10]. The comparative analysis of the phosphates and oxides/hydroxides is of significance to obtain insight into the synergistic effect of nickel and manganese on the capacitive performance of electrodes.

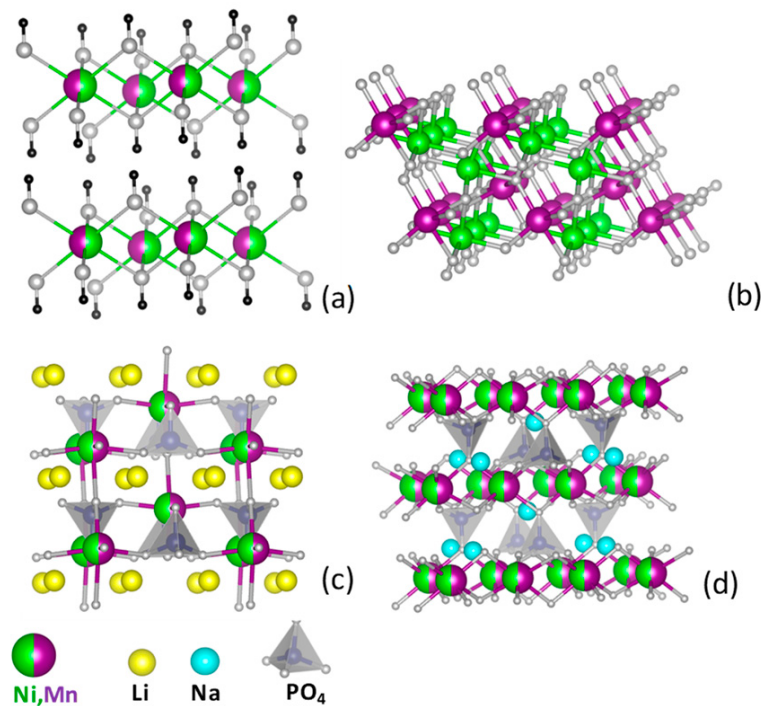


**Figure 1.** Schematic view of the crystal structures of mixed Ni–Mn phases: (a)  $\beta\text{-Ni}_{1/2}\text{Mn}_{1/2}(\text{OH})_2$ ; (b)  $\text{NiMnO}_3$ ; (c)  $\text{LiNi}_{1/2}\text{Mn}_{1/2}\text{PO}_4$ ; and (d)  $\text{NaNi}_{1/2}\text{Mn}_{1/2}\text{PO}_4$ . The structures are adopted from:  $\beta\text{-Ni}(\text{OH})_2$  (COD 9011314), ilmenite (ICSD 31853), phospho-olivine (COD 4002560) and maricite (COD 1530437).

## 2. Results and Discussion

For the preparation of single phases containing both nickel and manganese, specific synthetic procedures were adopted. Table 1 summarizes all the experimental conditions necessary for the synthesis of the given electrode, as well as its notation. Mixed nickel-manganese hydroxide,  $\text{Ni}_{1/2}\text{Mn}_{1/2}(\text{OH})_2$ , is prepared by the co-precipitation of a nickel-manganese aqueous solution with KOH. Interestingly, the kind of the used Ni and Mn salts affects the composition of the precipitated hydroxides (Figure S1); single  $\text{Ni}_{1/2}\text{Mn}_{1/2}(\text{OH})_2$  phase, which is isostructural to the well-known  $\beta\text{-Ni}(\text{OH})_2$  (Figure 1a, ICSD 28101), is obtained only in the case when nickel and manganese nitrate salts are used. The nickel and manganese sulfate salts yield a phase mixture between  $\alpha$ - and  $\beta$ -type  $\text{Ni}_x\text{Mn}_{1-x}(\text{OH})_2$ , as well as individual  $\text{Mn}(\text{OH})_2$  and  $\beta\text{-Ni}(\text{OH})_2$  (Figure S1). In this study, single  $\beta\text{-Ni}_{1/2}\text{Mn}_{1/2}(\text{OH})_2$  phase was only tested as an electrode in a supercapacitor cell. Contrary to the hydroxides, precipitation in the presence of  $\text{CO}_2$  leads to the formation of a single carbonate phase,  $\text{Ni}_{1/2}\text{Mn}_{1/2}\text{CO}_3$ , irrespective of the kind of the used nickel and manganese salts. The common features of  $\beta\text{-Ni}_{1/2}\text{Mn}_{1/2}(\text{OH})_2$  and  $\text{Ni}_{1/2}\text{Mn}_{1/2}\text{CO}_3$  are the random distributions of  $\text{Ni}^{2+}$  and  $\text{Mn}^{2+}$  ions in hydroxide and carbonate crystal structures (Figure S1).

**Table 1.** Experimental conditions, preparation methods, phase compositions and labeling of the studied hydroxides, oxides and phosphates.

Sample	Description	Preparation Method	T, °C	Annealing Time, hs	Phase Composition	Labeling
1	Ni–Mn hydroxide	Co-precipitation from nitrate salts	25	-	$\beta$ -type $\text{Ni}_{0.5}\text{Mn}_{0.5}(\text{OH})_2$	N-OH
2	Ni–Mn oxide	Thermal decomposition of hydroxides prepared from nitrates	400	3	Mixture of ilmenite $\text{NiMnO}_3$ and spinel $\text{Ni}_{1.5}\text{Mn}_{1.5}\text{O}_4$	IS-O
3	Ni–Mn oxide	Thermal decomposition of $\text{Ni}_{1/2}\text{Mn}_{1/2}\text{CO}_3$	400	3	Single ilmenite $\text{NiMnO}_3$ phase	I-O
4	Li–Ni–Mn phosphate	Li–Ni–Mn phosphate-formate precursor	500	10	Single olivine phase $\text{LiNi}_{1/2}\text{Mn}_{1/2}\text{PO}_4$	LP
5	Na–Ni–Mn phosphate	Na–Ni–Mn phosphate-formate precursor	700	10	Single maricite phase $\text{NaNi}_{1/2}\text{Mn}_{1/2}\text{PO}_4$	NP

Oxide electrodes are prepared by the thermal decomposition of the corresponding carbonate and hydroxide phases (Figure S1, Table 1). Although thermal decomposition of the carbonate phase,  $\text{Ni}_{1/2}\text{Mn}_{1/2}\text{CO}_3$ , yields single  $\text{NiMnO}_3$  phase with an ilmenite type of structure (Figure 1b, ICSD 31853), a mixture between oxide phases with ilmenite and spinel structures (i.e.,  $\text{NiMnO}_3$  and  $\text{Ni}_{1.5}\text{Mn}_{1.5}\text{O}_4$ ) is formed after the decomposition of a single  $\beta\text{-Ni}_{1/2}\text{Mn}_{1/2}(\text{OH})_2$  phase. As electrodes in a supercapacitor cell,  $\text{NiMnO}_3$  ilmenite and an oxide mixture, “ $\text{NiMnO}_3+\text{Ni}_{1.5}\text{Mn}_{1.5}\text{O}_4$ ”, are used.

The phosphate phases  $\text{LiNi}_{1/2}\text{Mn}_{1/2}\text{PO}_4$  and  $\text{NaNi}_{1/2}\text{Mn}_{1/2}\text{PO}_4$  are obtained from the lithium and sodium phosphate-formate precursors. XRD patterns evidence that lithium and sodium compounds crystallize in different types of structures, although the same synthetic method (Figure S1):  $\text{LiNi}_{1/2}\text{Mn}_{1/2}\text{PO}_4$  adopts an olivine-type structure (Figure 1c), whereas  $\text{NaNi}_{1/2}\text{Mn}_{1/2}\text{PO}_4$  crystallizes in a maricite-type structure (Figure 1d). The olivine- and maricite-type structures are closely related to each other; they have the same  $\text{PO}_4$  framework but with a reverse distribution of  $\text{M}^+$  and  $\text{M}^{2+}$  ions over the two octahedral sites ( $4a$  and  $4c$ ) [32,33]. It is of importance that  $\text{Ni}^{2+}$  and  $\text{Mn}^{2+}$  ions are randomly distributed on the given octahedral positions in the two structures, as discussed in the supporting information.

Specific surface area is another important factor contributing to the electrochemical performance of materials [34,35]. Figure 2 compares the specific surface area for all the samples. Hydroxides, oxides and phosphates are typical mesoporous materials (Figure 2). For  $\beta\text{-Ni}_{0.5}\text{Mn}_{0.5}(\text{OH})_2$  and its oxide-derived product (IS-O), the isotherms show characteristic H1-type hysteresis loops associated with the narrow distribution of relatively uniform cylindrical-like pores (Figure 2a,c) [36]. The calculated specific surface areas, total pore volumes and pore size distributions are collected in Table 2. The hydroxides and oxides have close porous characteristics with high specific surface areas (varying between 106 and  $128 \text{ m}^2 \text{ g}^{-1}$ ) and total pore volumes (i.e., varying between  $0.25$  and  $0.35 \text{ cm}^3 \text{ g}^{-1}$ ). However, close inspection of the pore size distribution curves (Figure 2 and Table 2) reveals that the mean pore size was slightly shifted after the thermal decomposition of the hydroxide to an oxide (i.e., from 8 to 11 nm). This means that the  $\text{H}_2\text{O}$  evolution from a hydroxide caused an opening of pores in the mesopore range. The phosphates exhibited low specific surface areas:  $7 \text{ m}^2 \text{ g}^{-1}$  for  $\text{LiNi}_{1/2}\text{Mn}_{1/2}\text{PO}_4$  and about  $1 \text{ m}^2 \text{ g}^{-1}$  for  $\text{NaNi}_{1/2}\text{Mn}_{1/2}\text{PO}_4$  (Table 2). (For the sake of convenience, the isotherm of  $\text{NaNi}_{1/2}\text{Mn}_{1/2}\text{PO}_4$  is not shown due to its lowest specific surface area.) For lithium compounds, the pores were distributed in a broad range from 5 to 100 nm, with mesopores with sizes between 10 and 50 nm being predominant. The different porosity of hydroxides/oxides and phosphates is related with the preparation conditions; phosphates are prepared at higher temperatures using longer heating times in comparison with oxides (Table 1).

**Table 2.** Specific surface area  $S_{\text{BET}}$ , total pore volume  $V_t$  and pore size distribution for the studied compounds.

Samples	Detailed Description	$S_{\text{BET}}, \text{m}^2 \text{ g}^{-1}$	$V_t, \text{cm}^3 \text{ g}^{-1}$	Pore size Distribution, nm
N-OH	$\beta\text{-Ni}_{1/2}\text{Mn}_{1/2}(\text{OH})_2$	117	0.25	Uniform narrow pore size distribution between 3 and 12 nm; mean pore size of 8 nm
I-O	$\text{NiMnO}_3$	128	0.35	Narrow pore size distribution between 3 and 12 nm; mean pore size of 10 nm
IS-O	$\text{NiMnO}_3 + \text{Ni}_{1.5}\text{Mn}_{1.5}\text{O}_4$	106	0.30	Uniform narrow pore size distribution between 3 and 18 nm; mean pore size of 11 nm
LP	$\text{LiNi}_{1/2}\text{Mn}_{1/2}\text{PO}_4$	7	0.04	Broad pore size distribution between 5 and 100 nm, with mesopores between 10 and 50 nm being predominant
NP	$\text{NaNi}_{1/2}\text{Mn}_{1/2}\text{PO}_4$	$\approx 1$	-	-

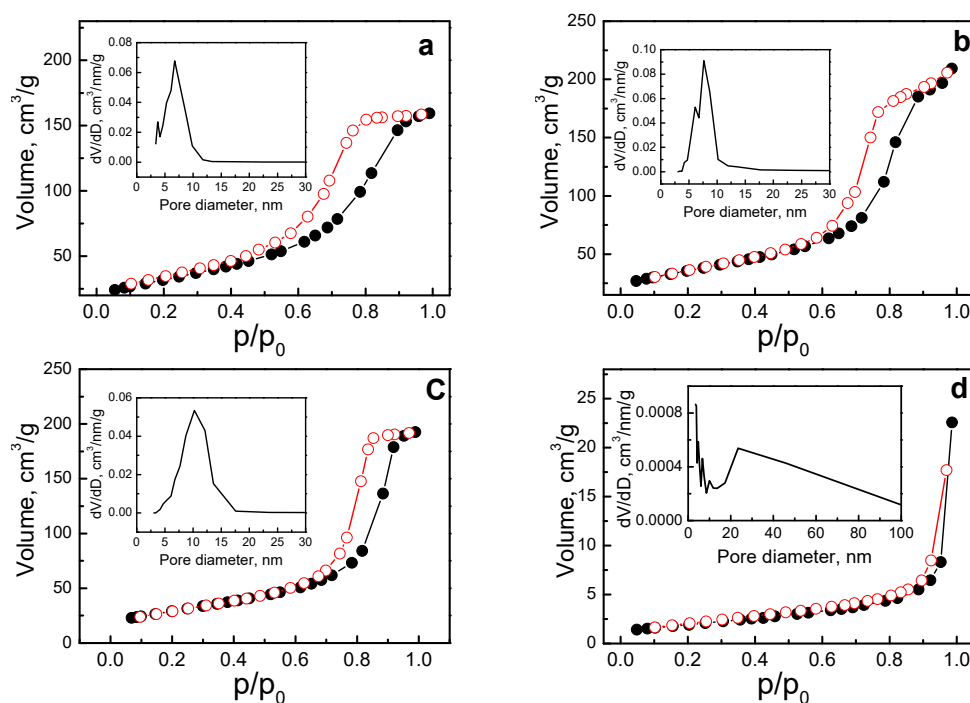


**Figure 2.** Adsorption–desorption isotherms of: (a)  $\beta\text{-Ni}_{1/2}\text{Mn}_{1/2}(\text{OH})_2$ ; (b) ilmenite NiMnO<sub>3</sub>; (c) mixture of NiMnO<sub>3</sub> and Ni<sub>1.5</sub>Mn<sub>1.5</sub>O<sub>4</sub>; and (d) LiNi<sub>1/2</sub>Mn<sub>1/2</sub>PO<sub>4</sub>. Filled and open symbols denote adsorption and desorption curves, respectively. The insets show the pore size distribution curves.

In synchrony with the porosity, the morphology of the samples is also specific. The morphology consisted of micrometric aggregates with various shapes (Figure 3). For NiMnO<sub>3</sub>, spherical aggregates with sizes of around 1–5  $\mu\text{m}$  dominated, whereas for  $\beta\text{-Ni}_{1/2}\text{Mn}_{1/2}(\text{OH})_2$  and its oxide-derivative, unshaped aggregates with sizes larger than 10  $\mu\text{m}$  appeared. For NaNi<sub>1/2</sub>Mn<sub>1/2</sub>PO<sub>4</sub>, having a lower specific surface area, primary well-shaped particles inside aggregates could be distinguished, with the particle dimensions being of 0.4–0.8  $\mu\text{m}$ . For LiNi<sub>1/2</sub>Mn<sub>1/2</sub>PO<sub>4</sub>, spherical aggregates were mostly observed.

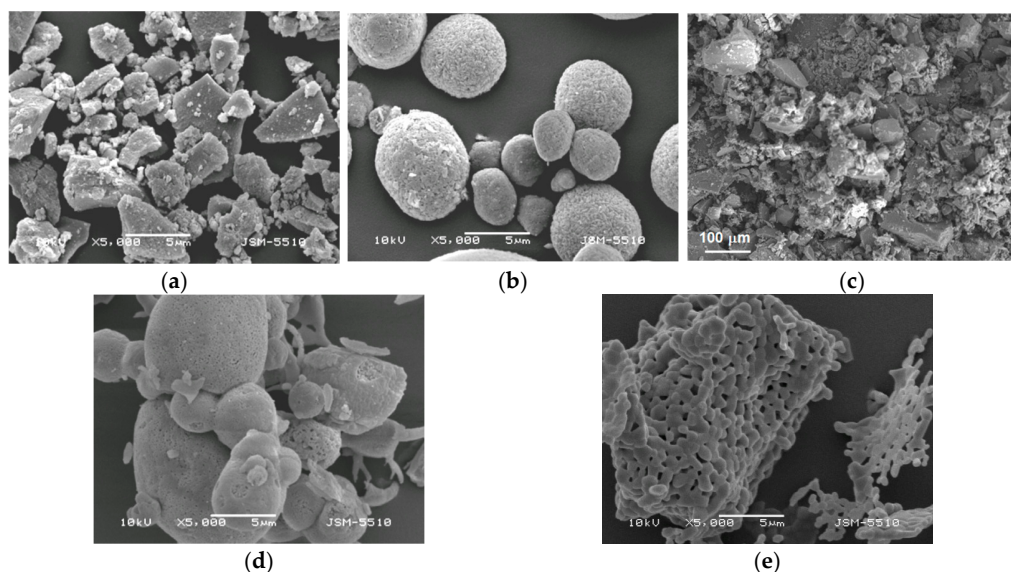


**Figure 3.** SEM images: (a)  $\beta\text{-Ni}_{1/2}\text{Mn}_{1/2}(\text{OH})_2$ ; (b) ilmenite NiMnO<sub>3</sub>; (c) mixture of NiMnO<sub>3</sub> and Ni<sub>1.5</sub>Mn<sub>1.5</sub>O<sub>4</sub>; (d) olivine LiNi<sub>1/2</sub>Mn<sub>1/2</sub>PO<sub>4</sub>; and (e) maricite NaNi<sub>1/2</sub>Mn<sub>1/2</sub>PO<sub>4</sub>.

All the samples used as positive electrodes in asymmetric electrochemical cells displayed charge/discharge curves whose shapes are typical for supercapacitor behavior [5–9] (Figure 4). The comparison shows that hydroxides, oxides and phosphates delivered different capacitances, with the highest being for ilmenite I-O and the lowest being for olivine LP. This reflects a current-resistance  $iR$  drop calculated from the discharge curve. I-O exhibited the lowest  $iR$  drop (i.e., drop in voltage  $\Delta V$  of  $0.029 \pm 0.002$  V at  $240 \text{ mA g}^{-1}$ ), and the highest value was calculated for LP (i.e., drop in voltage  $\Delta V$  of  $0.045 \pm 0.002$  V at  $240 \text{ mA g}^{-1}$ ).

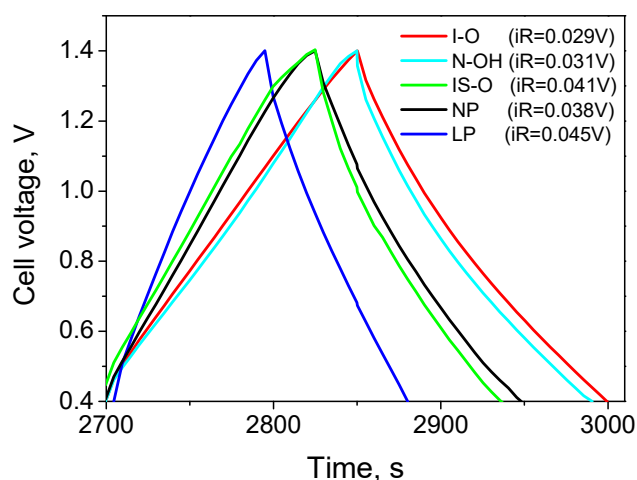


**Figure 4.** Galvanostatic charge–discharge curves of supercapacitor cells with different composite electrodes at a current load of  $240 \text{ mA g}^{-1}$ . The drop in voltage  $\Delta V$  (i.e.,  $iR$ ) is shown.

To more precisely compare the electrochemical performances of all the samples, two experimental protocols are used. Firstly, the electrochemical cells are cycled at a constant current load that increases stepwise from  $30$  to  $900 \text{ mA g}^{-1}$  for  $25$  cycles per each step (Figure 5). Secondly, the electrochemical cells are tested at a current load of  $240 \text{ mA g}^{-1}$  for  $5000$  cycles (Figure 6). According to the first protocol, the highest capacitance is delivered by the ilmenite oxide I-O regardless of the current load, with  $175 \text{ F g}^{-1}$  and  $115 \text{ F g}^{-1}$  at a current load of  $30$  and  $900 \text{ mA h g}^{-1}$ , respectively (Figure 5). The hydroxide N-OH displays lower capacitance than that of the ilmenite oxide I-O at a low current load, whereas at high current loads, the capacitances of hydroxides and oxides become comparable. This reveals a better rate performance of the hydroxides in comparison with that of the oxides. To understand the effect of the mixing of Ni and Mn, Figure 5 gives the capacitance behavior of  $\alpha,\beta\text{-Ni(OH)}_2$  reference, for which it has been shown to display the best performance among nickel hydroxide modifications [9]. This comparison indicates high capacitance values for mixed  $\beta\text{-Ni}_{1/2}\text{Mn}_{1/2}(\text{OH})_2$  hydroxide at lower current loads, whereas at high current loads, the capacitances of  $\beta\text{-Ni}_{1/2}\text{Mn}_{1/2}(\text{OH})_2$  and  $\alpha,\beta\text{-Ni(OH)}_2$  tend towards each other. When a spinel oxide  $\text{Ni}_{1.5}\text{Mn}_{1.5}\text{O}_4$  is mixed with ilmenite oxide  $\text{NiMnO}_3$  (IS-O), there is a decrease in the capacitance, thus indicating worse supercapacitor behavior of the spinel. It is worth mentioning that the better performance of ilmenite  $\text{NiMnO}_3$  compared to that of the spinel with a composition of  $\text{NiMn}_2\text{O}_4$  has been previously established [14]. Given that both oxides have close specific surface areas, the different capacitances disclose the effect of crystal structures on the supercapacitor behavior of oxides. This is more evidence for the complex features of energy storage for oxides, including capacitive and faradaic mechanisms. That is why the energy storage of oxides is calculated and presented in Figure 5 with units of  $\text{F g}^{-1}$  and  $\text{mA h g}^{-1}$ .

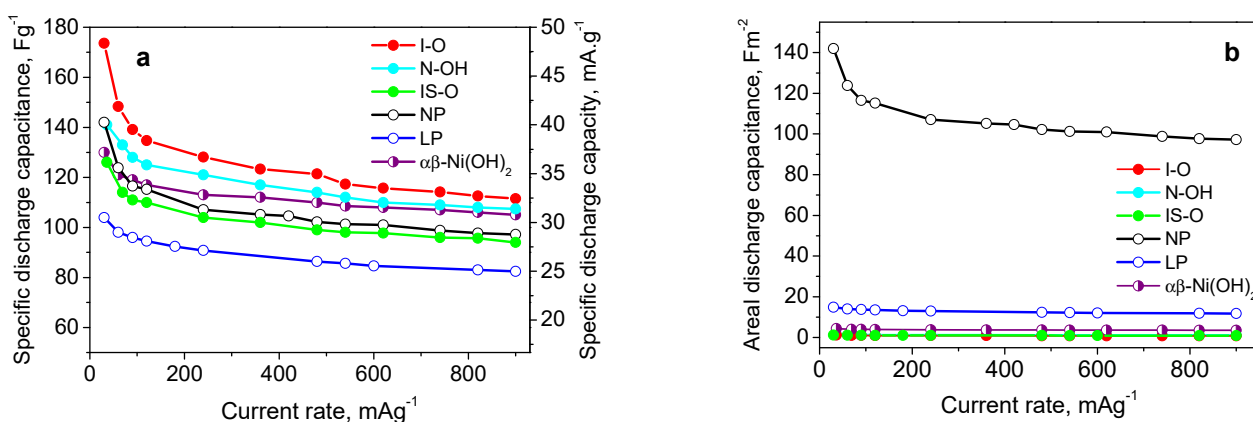


**Figure 5.** Specific discharge capacitance (a) and areal discharge capacitance (b) as a function of the current load of supercapacitor cells with different composite electrodes. For the sake of comparison, the discharge capacitance is also calculated in  $\text{mA h g}^{-1}$ .

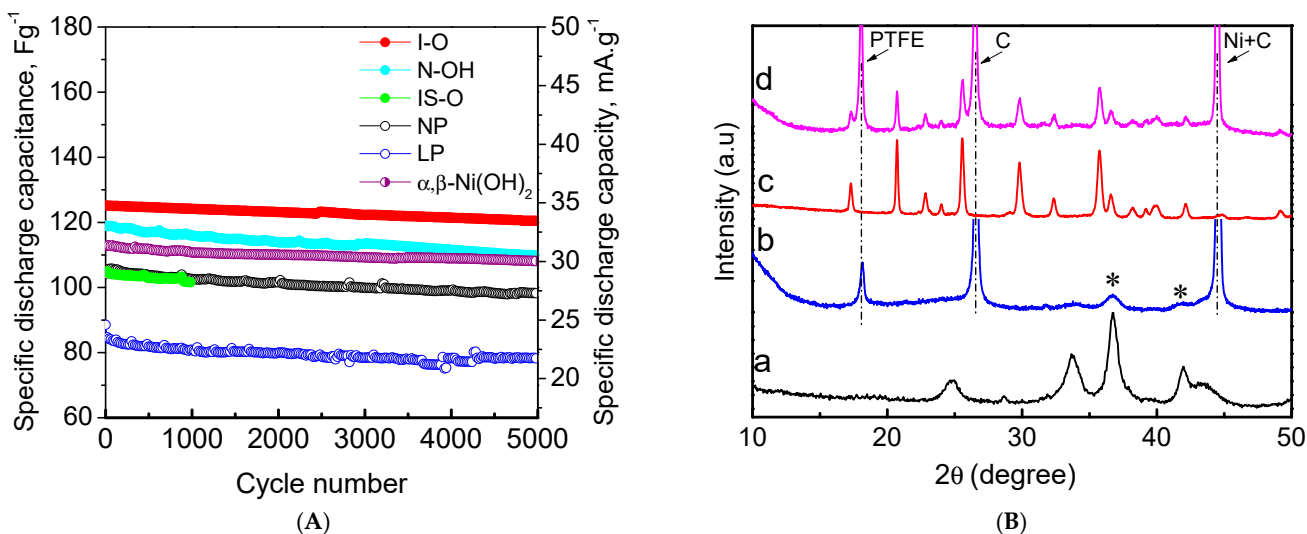


**Figure 6.** (A) Specific discharge capacitance (capacity) as a function of the cycle number at  $240 \text{ mA g}^{-1}$  of supercapacitor cells with different composite electrodes. (B) Ex situ XRD patterns of ilmenite (b) and phospho-olivine (d) electrodes after 5000 cycles. For the sake of comparison, the pristine ilmenite (a) and phospho-olivine (c) are also given. Symbols (\*), (PTFE), (C) and (Ni) denote the peaks due to the ilmenite phase, PTFE, graphite and Ni foam, respectively.

The lowest capacitance was observed for the olivine LP, with  $105 \text{ F g}^{-1}$  and  $90 \text{ F g}^{-1}$  at a current load of 30 and  $900 \text{ mA h g}^{-1}$ , respectively. However, the olivine LP outperformed the oxides and hydroxides with respect to the rate capability. Going from 30 to  $900 \text{ mA g}^{-1}$ , the capacitance loss was around  $50 \text{ F g}^{-1}$  for I-O and only  $15 \text{ F g}^{-1}$  for LP. Irrespective of the lowest specific surface area, the maricite NP demonstrated a capacitance that was close to that of the mixed oxide “ilmenite-spinel”. To outline the performance of maricite NP, the discharge capacitance was calculated per specific surface area (Figure 5). According to this scheme, the maricite NP delivered the highest areal capacitance, followed by the phospho-olivine (Figure 5). On one hand, this illustrates the impact of the crystal structure on the supercapacitor behavior of phosphates, which mimics that of the oxides. On the other hand, the maricite NP may be of interest as an electrode material in hybrid supercapacitors if its specific surface area is increased drastically.

The second protocol of electrochemical testing is based on an extended number of cycles, and it enables the further differentiation of samples as electrode materials (Figure 6A). After 5000 cycles, the ilmenite I-O delivered the highest capacitance (i.e., of around

$125 \text{ F g}^{-1}$ ) and better cycling stability (i.e., around of 96%). The oxide mixture between ilmenite and spinel underperforms the single ilmenite phase, thus supporting once again the better capacitive performance of the ilmenite phase. The N-OH hydroxide is characterized by a slightly lower capacitance than that of ilmenite I-O (i.e., around of  $115 \text{ F g}^{-1}$ ), but the cycling stability was worse (around 92%). It is noticeable that  $\alpha,\beta\text{-Ni(OH)}_2$  reference, having a lower capacitance than that of N-OH ( $113$  versus  $119 \text{ F g}^{-1}$ ), displayed better cycling stability (i.e., around 95%). In comparison with oxides and hydroxides, the performance of the phosphate electrodes was worse; the capacitance was lower than  $100 \text{ F g}^{-1}$ , and the cycling stability tended to 92% regardless of the crystal structure (i.e., maricite or olivine). It is of importance that the capacitances of mixed Ni-Mn phosphates are among the highest values reported in the literature, in which single Mn and Ni phosphates are mainly examined [23–29]. Moreover, single maricite phosphate NP and mixed ilmenite and spinel oxides IS-O had comparable capacitances regardless of their different specific surface areas (Table 2). The above data allow the outlining of two important features; the capacitance depends mainly on whether the electrode simultaneously contains nickel and manganese and, to a lesser extent, on the type of anionic constituents. On the other hand, the cycling stability is a function of the morphology; it appears that better cycling stability is achieved at spherical aggregates.

Cycling stability is directly associated with the chemical stability of electrodes in alkaline electrolytes. For that reason, Figure 6B gives the ex situ XRD patterns of ilmenite and phospho-olivine after 5000 cycles at  $240 \text{ mA g}^{-1}$ . These electrodes were selected since they exhibit the best and worst performances. As one can see, both XRD patterns remained unchanged, thus indicating the chemical stability of the ilmenite and phospho-olivine phases during cycling in alkaline electrolytes.

To rationalize the electrochemical performance of oxides, hydroxides and phosphates, Figure 7 compares the relationship between energy density and power density. For the sake of comparison, the data available in the literature are also given. At lower power densities, the specific energy density decreases in following the order: I-O > N-OH~NP >  $\alpha,\beta\text{-Ni(OH)}_2$  > LP, whereas at a high power density, the specific energy of I-O, N-OH and  $\alpha,\beta\text{-Ni(OH)}_2$  becomes close and higher than that of the phosphates. It is of importance that the ilmenite  $\text{NiMnO}_3$  still displays a high energy density at the highest power density (i.e.,  $65 \text{ W h kg}^{-1}$  at  $3200 \text{ W kg}^{-1}$ ).

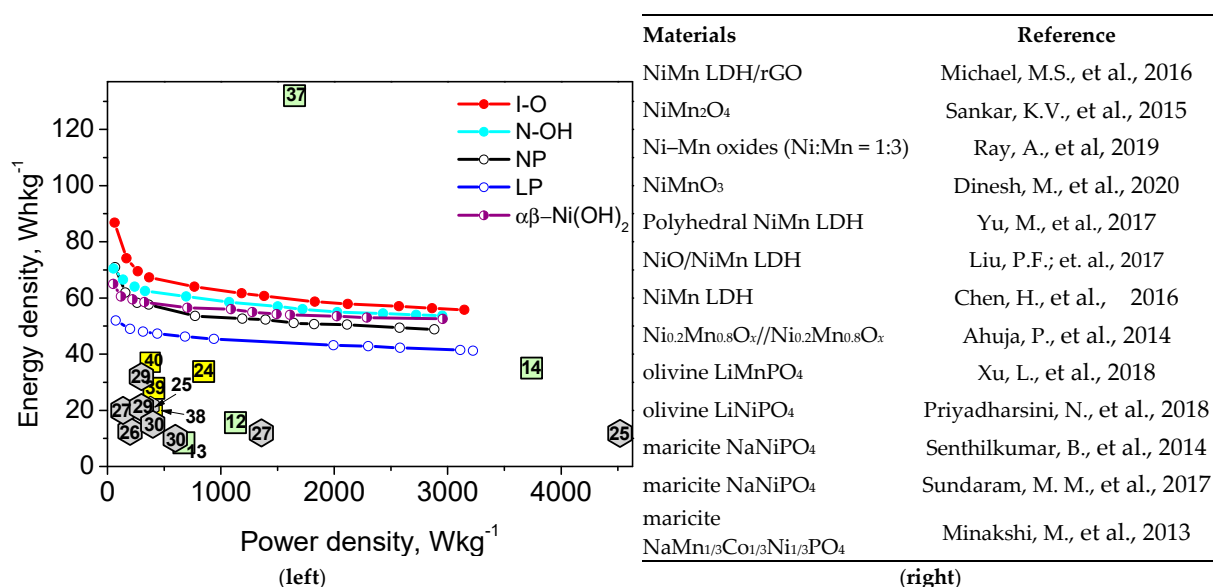


**Figure 7.** (left) Energy density versus power density (Ragone plot) for supercapacitors with different composite electrodes. The literature data for oxides, hydroxides and phosphates are indicated as ■, ▲ and ▽, respectively (right). The used references are given in the figure: [12–14,24–27,29,30,37–40].

This can be related with the synergistic effect of Ni and Mn elements, as well as with the specific morphology and texture of I-O. The capacitance performance of ilmenite I-O is one of the good performances reported in literature (Figure 7). In comparison with ilmenite I-O with a Ni-to-Mn ratio of one-to-one, composite  $\text{Ni}_{0.2}\text{Mn}_{0.8}\text{O}_x/\text{Ni}_{0.2}\text{Mn}_{0.8}\text{O}_x$  oxides with a Ni-to-Mn ratio of one-to-four exhibit an energy density of around  $38 \text{ W h kg}^{-1}$  at  $3800 \text{ W kg}^{-1}$  power density, whereas the energy and the power density of Ni–Mn oxide with a one-to-three ratio reach around  $130 \text{ W h kg}^{-1}$  at  $1700 \text{ W kg}^{-1}$  [23,26]. The ilmenite  $\text{NiMnO}_3$  prepared by the hydrothermal method displays significantly lower energy density (i.e., around  $10 \text{ W h kg}^{-1}$  at  $700 \text{ W kg}^{-1}$  [22]) than that of ilmenite  $\text{NiMnO}_3$  prepared by us using the co-precipitation method. Interestingly, the hydrothermal-derived  $\text{NiMnO}_3$ , having worse performance, is characterized by a low specific surface area (i.e., around  $21 \text{ m}^2 \text{ g}^{-1}$ ) and irregularly shaped particles with a size of 100–200 nm, whereas co-precipitate-derived  $\text{NiMnO}_3$ , having the best performance, possesses a high specific surface area (around  $125\text{--}130 \text{ m}^2 \text{ g}^{-1}$ ) and spherical morphology. It is well recognized that spherical morphology is an important factor contributing to the improved performance of battery-like materials due to a higher volume-to-surface ratio of the electrode and its better wetting with electrolytes [41]. Given that the energy storage mechanism of Ni–Mn oxides in supercapacitors is more complex than the single capacitive and faradaic one, it is not surprising that spherical morphology has a favorable effect in asymmetric supercapacitors too.

Both LP and NP phosphates deliver lower specific energy densities than those of oxides and hydroxides (Figure 7), with NP being slightly better than LP. Keeping a Ni-to-Mn ratio of one-to-one, this implies, at first glance, that the capacitive performance of an electrode depends further on the anionic constituents and on the type of structure. Considering that the morphology of phosphates is not optimized, it appears that the phosphates are also suitable for supercapacitor applications. Moreover, the energies and power densities of the phosphates prepared by us, which simultaneously contained Ni and Mn, were more than two times higher than those of phosphates containing one element, such as Ni or Mn (Figure 7). This supports once again the leading effect of Ni and Mn elements on the performance of electrodes in hybrid supercapacitors.

### 3. Conclusions

Three types of electrodes were evaluated in hybrid supercapacitor cells with alkaline electrolytes: oxides with ilmenite and spinel structures, hydroxides isostructural to  $\beta\text{-Ni(OH)}_2$  and phosphates with olivine and maricite structures. The common feature between them is that their crystal structures are able to simultaneously accommodate nickel and manganese ions. The capacitance performances of oxides, hydroxides and phosphates depend mainly on whether the electrode contains simultaneously nickel and manganese in a ratio of one-to-one and, to a lesser extent, on the type of anionic constituents. Cycling stability becomes better when the morphology consists of spherical aggregates. Based on these findings, one can predict the electrode with the best capacitance performance; the electrode composition should simultaneously contain Ni and Mn ions, and the morphology should comprise spherical aggregates. A proof-of-concept is demonstrated by  $\text{NiMnO}_3$  with an ilmenite structure and optimized morphology; it delivers high energy and power density (i.e.,  $65 \text{ W h kg}^{-1}$  at  $3200 \text{ W kg}^{-1}$ ) and exhibits good cycling stability (i.e., around 96% after 5000 cycles at a current load of  $240 \text{ mA g}^{-1}$ ). The capacitive performance of olivine and maricite phosphates outperforms the previously reported phosphates by more than two times due to the synergistic effect of  $\text{Ni}^{2+}$  and  $\text{Mn}^{2+}$  ions. Further optimization of phosphate morphology is needed in order to reach the capacitance performance of  $\text{NiMnO}_3$  ilmenite.

## 4. Material and Methods

### 4.1. Synthesis

The mixed Ni–Mn hydroxides were prepared via the classical co-precipitation method from nickel and manganese salts (1:1 mole ratio) and KOH as a precipitant. Two kinds of salts were used: nitrates and sulfates. The mixed Ni–Mn oxides were obtained by the thermal decomposition of the following at 400 °C: (i) corresponding hydroxides; (ii) calcite-type  $\text{Ni}_{1/2}\text{Mn}_{1/2}\text{CO}_3$  prepared by a co-precipitation from the nitrate salts with  $\text{NaHCO}_3$  in a flow of  $\text{CO}_2$ . For the synthesis of  $\text{LiNi}_{1/2}\text{Mn}_{1/2}\text{PO}_4$  and  $\text{NaNi}_{1/2}\text{Mn}_{1/2}\text{PO}_4$ , we adopted the phosphate-formate precursor method developed previously for the preparation of electrochemically active  $\text{LiMPO}_4$  ( $M = \text{Fe}, \text{Mn}, \text{Co}, \text{Ni}$ ) and  $\text{NaMPO}_4$  [32,33]. The synthetic procedure consists of mixing aqueous solutions of  $\text{Ni}(\text{HCOO})_2 \cdot 2\text{H}_2\text{O}$ ,  $\text{Mn}(\text{HCOO})_2 \cdot 2\text{H}_2\text{O}$  and  $\text{LiH}_2\text{PO}_4$ , accordingly  $\text{NaH}_2\text{PO}_4$ , taken in a mole ratio of 1:1:2. The metal-phosphate-formate solutions were frozen instantly with liquid nitrogen and subjected to freeze-drying for about 18 h in vacuum (20–30 mbar) using an Alpha-Christ Freeze Dryer. Thus, the obtained solid phosphate-formate precursors were pre-decomposed in an air atmosphere at 350 °C for 4 h. The solid products were further annealed at temperatures between 500 and 700 °C.

### 4.2. Characterization Methods

The XRD patterns of the oxides/hydroxides and phosphates were recorded on a Bruker D8 Advance diffractometer using  $\text{CuK}\alpha$  radiation (LynxEye detector). The Ni and Mn contents in the mixed composition were determined by inductively coupled plasma atomic emission spectrometry (ICP-AES). The morphology of the electrode materials was examined by JEOL JSM-5510 SEM. The porous texture of the samples was studied by low-temperature (77.4 K) nitrogen adsorption using the Quantachrome (Boynton Beach, FL, USA) NOVA 1200e instrument. The specific surface area was evaluated by the BET method at a relative pressure  $p/p_0$  in a range of 0.10–0.30. The total pore volume was calculated according to Gurwitsch's rule at  $p/p_0 = 0.99$ . The pore size distribution was estimated by using the Barett–Joyner–Halenda method.

### 4.3. Electrochemical Characterization

Two-electrode cells were used to monitor the electrochemical performances of the electrodes. The cell was constructed from a positive electrode (consisting of a mixture between activated carbon (AC) and oxides/hydroxides in a content of 25 wt.%) and a negative electrode (containing only AC) with the mass ratio between them being 1:1. As a binder and a conductive additive, we used polytetrafluoroethylene (PTFE) (10 wt.%) and graphite ABG 1005 EG1 (10 wt.%). The electrolyte contained 7 M KOH solutions with additives of 35 g l-1 LiOH. The charge–discharge curves were recorded on the Arbin Instrument System BT-2000. The capacitance ( $\text{F g}^{-1}$ ) was calculated from the charge–discharge curves using the following equations [42,43]:

$$C = (I \times \Delta t) / (m \times \Delta V) \quad (1)$$

where  $I$  (A),  $\Delta t$  (s),  $m$  (g) and  $\Delta V$  (V) are the discharge current, discharge time, mass of the active material and voltage window, respectively. Based on the capacitance, the energy densities ( $E$ ,  $\text{W h kg}^{-1}$ ) and power densities ( $P$ ,  $\text{W kg}^{-1}$ ) were calculated as [44]:

$$E = C \Delta V^2 / 2 \quad (2)$$

$$P = E \times 3600 / t \quad (3)$$

**Supplementary Materials:** The following supporting information can be downloaded at: <https://www.mdpi.com/article/10.3390/batteries8060051/s1>. Figure S1: XRD patterns of Ni–Mn-based mixed hydroxides, oxides and phosphates. References [27,32,33,45–47] are cited in the supplementary materials.

**Author Contributions:** Conceptualization, R.S.; methodology, V.K., A.S. and R.S.; validation, L.S. and D.M.; investigation, L.S., D.M. and V.K.; data curation, L.S. and D.M.; writing—original draft preparation, V.K., A.S. and R.S.; writing—review and editing, R.S., V.K. and A.S.; visualization, V.K. and L.S.; project administration, A.S. and R.S.; funding acquisition, A.S. All authors have read and agreed to the published version of the manuscript.

**Funding:** This research was funded by the Bulgarian National Science Fund, grant number KP-06-OOPR 04/5 “Innovative hybrid supercapacitors as a challenge for efficient, safe and environmental energy storage” and by the Operational Programme “Science and Education for Smart Growth” 2014–2020, co-funded by the EU from the European Regional Development Fund, grant number No BG05M2OP001-1.001-0008.

**Institutional Review Board Statement:** Not applicable.

**Informed Consent Statement:** Not applicable.

**Data Availability Statement:** Not applicable.

**Conflicts of Interest:** The authors declare no conflict of interest. The funders had no role in the design of the study; in the collection, analyses or interpretation of the data; in the writing of the manuscript; or in the decision to publish the results.

## References

- Choi, C.; Ashby, D.S.; Butts, D.M.; DeBlock, R.H.; Wei, G.; Lau, J.; Dunn, B. Achieving high energy density and high power density with pseudocapacitive materials. *Nat. Rev. Mater.* **2020**, *5*, 5–19. [[CrossRef](#)]
- Chatterjee, D.; Nandi, A. A review on the recent advances in hybrid supercapacitors. *J. Mater. Chem. A* **2021**, *9*, 15880–15918. [[CrossRef](#)]
- Xu, C.; Yang, H.; Li, Y.; Wang, J.; Lu, X. Surface engineering for advanced aqueous supercapacitors: A Review. *ChemElectroChem* **2020**, *7*, 586–593. [[CrossRef](#)]
- Zang, X.; Shen, C.; Sanghadasa, M.; Lin, L. High-voltage supercapacitors based on aqueous electrolytes. *ChemElectroChem* **2019**, *6*, 976–988. [[CrossRef](#)]
- Majumdar, D. Review on current progress of MnO<sub>2</sub>-based ternary nanocomposites for supercapacitor applications. *ChemElectroChem* **2021**, *8*, 291–336. [[CrossRef](#)]
- Hsieh, Y.-C.; Lee, K.-T.; Lin, Y.-P.; Wu, N.-L.; Donne, S.W. Investigation on capacity fading of aqueous MnO<sub>2</sub>·nH<sub>2</sub>O electrochemical capacitor. *J. Power Sources* **2008**, *177*, 660–664. [[CrossRef](#)]
- Guo, J.; Zhao, Y.; Jiang, N.; Liu, A.; Gao, L.; Li, Y.H.; Wang, H.; Ma, T. In-situ grown Ni(OH)<sub>2</sub> nanosheets on Ni foam for hybrid supercapacitors with high electrochemical performance. *J. Electrochem. Soc.* **2018**, *165*, A882. [[CrossRef](#)]
- Mozaffari, S.A.; Najafi, S.H.M.; Norouzi, Z. Hierarchical NiO@Ni(OH)<sub>2</sub> nanoarrays as high-performance supercapacitor electrode material. *Electrochim. Acta* **2021**, *368*, 137633. [[CrossRef](#)]
- Ramesh, S.; Karuppasamy, K.; Yadav, M.H.; Lee, J.-J.; Kim, H.-S.; Kim, H.-S.; Kim, J.-H. Ni(OH)<sub>2</sub>-decorated nitrogen doped MWCNT nanosheets as an efficient electrode for high performance supercapacitors. *Sci. Rep.* **2019**, *9*, 6034. [[CrossRef](#)]
- Sosorov, L.; Stoyanova, A.; Boyadzhieva, T.; Koleva, V.; Kalapsazova, M. Nickel-manganese structured and multiphase composites as electrodes for hybrid supercapacitors. *Electrochim. Acta* **2018**, *283*, 1063–1071. [[CrossRef](#)]
- Chen, D.; Wang, Q.; Wang, R.; Shen, G. Ternary oxide nanostructured materials for supercapacitors. *J. Mater. Chem. A* **2015**, *3*, 10158–10173. [[CrossRef](#)]
- Sankar, K.V.; Surendran, S.; Pandi, S.; Allin, M.; Nithya, V.D.; Lee, Y.S.; Selvan, R.K. Studies on the electrochemical intercalation/de-intercalation mechanism of NiMn<sub>2</sub>O<sub>4</sub> for high stable pseudocapacitor electrodes. *RSC Adv.* **2015**, *5*, 27649–27656. [[CrossRef](#)]
- Dinesh, M.; Haldorai, Y.; Thangavelu, R.; Kumar, R. Mn–Ni binary metal oxide for high-performance supercapacitor and electro-catalyst for oxygen evolution reaction. *Ceram. Int.* **2020**, *46*, 28006–28012. [[CrossRef](#)]
- Ahuja, P.; Ujjain, S.K.; Sharma, S.R.; Singh, G. Enhanced supercapacitor performance by incorporating nickel in manganese oxide. *RSC Adv.* **2014**, *4*, 57192–57199. [[CrossRef](#)]
- Li, M.; Cheng, J.P.; Wang, J.; Liu, F.; Zhang, X.B. The growth of nickel-manganese and cobalt-manganese layered double hydroxides on reduced graphene oxide for supercapacitor. *Electrochim. Acta* **2016**, *206*, 108–115. [[CrossRef](#)]
- Wang, R.; Wu, J. Structure and basic properties of ternary metal oxides and their prospects for application in supercapacitors. In *Metal Oxides in Supercapacitors*; Elsevier: Amsterdam, The Netherlands, 2017; pp. 99–132.
- Singh, A.K.; Sarkar, D.; Khan, G.G.; Mandal, K. Hydrogenated NiO nanoblock architecture for high performance pseudocapacitor. *ACS Appl. Mater. Interfaces* **2014**, *6*, 4684–4692. [[CrossRef](#)]

18. Lu, Q.; Lattanzi, M.W.; Chen, Y.P.; Kou, X.M.; Li, W.F.; Fan, X.; Unruh, K.M.; Chen, J.G.; Xiao, J.Q. Supercapacitor electrodes with high-energy and power densities prepared from monolithic NiO/Ni nanocomposites. *Angew. Chem. Int. Ed.* **2011**, *50*, 6847–6850. [[CrossRef](#)]
19. Li, X.; Xin, M.; Guo, S.; Cai, T.; Du, D.; Xing, W.; Zhao, L.; Guo, W.; Xue, Q.; Yan, Z. Insight of synergistic effect of different active metal ions in layered double hydroxides on their electrochemical behaviors. *Electrochim. Acta* **2017**, *253*, 302–310. [[CrossRef](#)]
20. Kim, H.; Hong, J.; Park, K.-Y.; Kim, H.; Kim, S.-W.; Kang, K. Aqueous rechargeable Li and Na ion batteries. *Chem. Rev.* **2014**, *114*, 11788–11827. [[CrossRef](#)]
21. Pang, H.; Yan, Z.; Wang, W.; Chen, J.; Zhang, J.; Zheng, H. Facile fabrication of  $\text{NH}_4\text{CoPO}_4 \cdot \text{H}_2\text{O}$  nano/microstructures and their primarily application as electrochemical supercapacitor. *Nanoscale* **2012**, *4*, 5946–5953. [[CrossRef](#)]
22. Li, X.; Xiao, X.; Li, Q.; Wei, J.; Xue, H.; Pang, H. Metal ( $M = \text{Co}, \text{Ni}$ ) phosphate based materials for high-performance supercapacitors. *Inorg. Chem. Front.* **2018**, *5*, 11–28. [[CrossRef](#)]
23. Prabaharan, S.R.S.; Anslin Star, R.; Kulkarni, A.R.; Michael, M.S. Nano-composite  $\text{LiMnPO}_4$  as new insertion electrode for electrochemical supercapacitors. *Curr. Appl. Phys.* **2015**, *15*, 1624–1633. [[CrossRef](#)]
24. Michael, M.S.; Kulkarni, A.R.; Prabaharan, S.R.S. Design of monolayer porous carbon-embedded hybrid- $\text{LiMnPO}_4$  for high energy density Li-ion capacitors. *J. Nanosci. Nanotechnol.* **2016**, *16*, 7314–7324. [[CrossRef](#)]
25. Xu, L.; Wang, S.; Zhang, X.; He, T.; Lu, F.; Li, H.; Ye, J. A facile method of preparing  $\text{LiMnPO}_4$ /reduced graphene oxide aerogel as cathodic material for aqueous lithium-ion hybrid supercapacitors. *Appl. Surf. Sci.* **2018**, *428*, 977–985. [[CrossRef](#)]
26. Priyadharsini, N.; Rupa Kasturi, P.; Shanmugavani, A.; Surendran, S.; Shanmugapriya, S.; Kalai Selvan, R. Effect of chelating agent on the sol-gel thermolysis synthesis of  $\text{LiNiPO}_4$  and its electrochemical properties for hybrid capacitors. *J. Phys. Chem. Solids* **2018**, *119*, 183–192. [[CrossRef](#)]
27. Senthilkumar, B.; Sankar, K.V.; Vasylechko, L.; Lee, Y.-S.; Selvan, R.K. Synthesis and electrochemical performances of maricite- $\text{NaMPO}_4$  ( $M = \text{Ni, Co, Mn}$ ) electrodes for hybrid supercapacitors. *RSC Adv.* **2014**, *4*, 53192–53200. [[CrossRef](#)]
28. Minakshi, M.; Mitchell, D.; Jones, R.; Alenazey, F.; Watcharatharapong, T.; Chakraborty, S.; Ahuja, R. Synthesis, structural and electrochemical properties of sodium nickel phosphate for energy storage devices. *Nanoscale* **2016**, *8*, 11291–11305. [[CrossRef](#)]
29. Sundaram, M.M.; Mitchell, D.R.G. Dispersion of  $\text{Ni}^{2+}$  ions via acetate precursor in the preparation of  $\text{NaNiPO}_4$  nanoparticles: Effect of acetate vs. nitrate on the capacitive energy storage properties. *Dalton Trans.* **2017**, *46*, 13704–13713. [[CrossRef](#)]
30. Minakshi, M.; Meyrick, D.; Appadoo, D. Maricite ( $\text{NaMn}_{1/3}\text{Ni}_{1/3}\text{Co}_{1/3}\text{PO}_4$ )/Activated carbon: Hybrid capacitor. *Energy Fuels* **2013**, *27*, 3516–3522. [[CrossRef](#)]
31. Sundaram, M.M.; Watcharatharapong, T.; Chakraborty, S.; Ahuja, R.; Duraisamy, S.; Rao, T.; Munichandraiah, N. Synthesis, and crystal and electronic structure of sodium metal phosphate for use as a hybrid capacitor in non-aqueous electrolyte. *Dalton Trans.* **2015**, *44*, 20108–20120. [[CrossRef](#)]
32. Koleva, V.; Stoyanova, R.; Zhecheva, E. Nano-crystalline  $\text{LiMnPO}_4$  prepared by a new phosphate-formate precursor method. *Mater. Chem. Phys.* **2010**, *121*, 370–377. [[CrossRef](#)]
33. Koleva, V.; Boyadzhieva, T.; Zhecheva, E.; Nihtanova, D.; Simova, S.; Tyuliev, G.; Stoyanova, R. Precursor-based methods for low-temperature synthesis of defectless  $\text{NaMnPO}_4$  with an olivine- and maricite-type structure. *Cryst. Eng. Comm.* **2013**, *15*, 9080–9089. [[CrossRef](#)]
34. Roberts, A.J.; Slade, R.C.T. Effect of specific surface area on capacitance in asymmetric carbon/ $\alpha\text{-MnO}_2$  supercapacitors. *Electrochim. Acta* **2010**, *55*, 7460–7469. [[CrossRef](#)]
35. Zheng, S.; Zhang, J.; Deng, H.; Du, Y.; Shi, X. Chitin derived nitrogen-doped porous carbons with ultrahigh specific surface area and tailored hierarchical porosity for high performance supercapacitors. *J. Bioresour. Bioprod.* **2021**, *6*, 142–151. [[CrossRef](#)]
36. Sing, K.S.W.; Williams, R.T. Physisorption hysteresis and the characterization of nanoporous materials. *Adsorpt. Sci. Technol.* **2004**, *22*, 773–782. [[CrossRef](#)]
37. Ray, A.; Roy, A.; Saha, S.; Ghosh, M.; Chowdhury, S.R.; Maiyalagan, T.; Bhattacharya, S.K.; Das, S. Das, Electrochemical energy storage properties of Ni-Mn-oxide electrodes for advance asymmetric supercapacitor application. *Langmuir* **2019**, *35*, 8257–8267.
38. Liu, P.F.; Zhou, J.J.; Li, G.C.; Wu, M.K.; Tao, K.; Yi, F.Y.; Zhao, W.N.; Han, L. A hierarchical  $\text{NiO}/\text{NiMn}$ -layered double hydroxide nanosheet array on Ni foam for high performance supercapacitors. *Dalton Trans.* **2017**, *46*, 7388–7391. [[CrossRef](#)]
39. Chen, H.; Ai, Y.; Liu, F.; Chang, X.; Xue, Y.; Huang, Q.; Wang, C.; Lin, H.; Han, S. Carbon-coated hierarchical Ni–Mn layered double hydroxide nanoarrays on Ni foam for flexible high-capacitance supercapacitors. *Electrochim. Acta* **2016**, *213*, 55–65. [[CrossRef](#)]
40. Bucher, N.; Hartung, S.; Nagasubramanian, A.; Cheah, Y.L.; Hostetler, H.E.; Madhavi, S. Layered  $\text{Na}_x\text{MnO}_{2+z}$  in sodium ion batteries—Influence of morphology on cycle performance. *ACS Appl. Mater. Interfaces* **2014**, *6*, 8059–8065. [[CrossRef](#)]
41. Yu, M.; Liu, R.; Liu, J.; Li, S.; Ma, Y. Polyhedral-like  $\text{NiMn}$ -layered double hydroxide/porous carbon as electrode for enhanced electrochemical performance supercapacitors. *Small* **2017**, *13*, 1702616. [[CrossRef](#)]
42. Wang, T.; Zhang, S.; Yan, X.; Lyu, M.; Wang, L.; Bell, J.; Wang, H. 2-Methylimidazole-derived Ni-Co layered double hydroxide nanosheets as high rate capability and high energy density storage material in hybrid supercapacitors. *ACS Appl. Mat. Interfaces* **2017**, *9*, 15510–15524. [[CrossRef](#)] [[PubMed](#)]
43. Khan, Y.; Hussain, S.; Söderlind, F.; Käll, P.-O.; Abbasi, M.A.; Durrani, S.K. Honeycomb  $\beta\text{-Ni(OH)}_2$  films grown on 3D nickel foam substrates at low temperature. *Mater. Lett.* **2012**, *69*, 37–40. [[CrossRef](#)]

44. Huang, J.; Xu, P.; Cao, D.; Zhou, X.; Wang, G. Asymmetric supercapacitors based on  $\beta$ -Ni(OH)<sub>2</sub> nanosheets and activated carbon with high energy density. *J. Power Sources* **2014**, *246*, 371–376. [[CrossRef](#)]
45. Pertlik, F. Structures of hydrothermally synthesized cobalt(II) carbonate and nickel(II) carbonate. *Acta Crystallogr. Sect. C Cryst. Struct. Commun.* **1986**, *42*, 4. [[CrossRef](#)]
46. Maslen, E.N.; Strel'tsov, V.A.; Strel'tsova, N.R.; Ishizawa, N. Electron density and optical anisotropy in rhombohedral carbonates. III. Synchrotron X-ray studies of CaCO<sub>3</sub>, MgCO<sub>3</sub> and MnCO<sub>3</sub>. *Acta Crystallogr. B* **1995**, *51*, 929–939. [[CrossRef](#)]
47. Koleva, V.; Zhecheva, E.; Stoyanova, R. Ordered Olivine-Type Lithium–Cobalt and Lithium–Nickel Phosphates Prepared by a New Precursor Method. *Eur. J. Inorg. Chem.* **2010**, *2010*, 4091–4099. [[CrossRef](#)]